This is a preprint, the final version is subject to change, of the American Mineralogist (MSA)
Cite as Authors (Year) Title. American Mineralogist, in press.
DOI: https://doi.org/10.2138/am-2019-6574

Revision 2.

Activation of [100](001) slip system by water incorporation in olivine and the cause of seismic anisotropy decrease with depth in the asthenosphere

Lin Wang[a,*], Nobuyoshi Miyajima[a], Takaaki Kawazoe[b], and Tomoo Katsura[a]

[a] Bayerisches Geoinstitut, University of Bayreuth, 95440 Bayreuth, Germany.

[b] Department of Earth and Planetary Systems Science, Hiroshima University, Japan

* Corresponding author.

E-mail address:

Lin Wang: lin.wang@uni-bayreuth.de

Nobuyoshi Miyajima: nobuyoshi.miyajima@uni-bayreuth.de

Takaaki Kawazoe: kawazoe@hiroshima-u.ac.jp

Tomoo Katsura: tomo.katsura@uni-bayreuth.de

Abstract

A transition from A-type to E-type fabrics in olivine may be the cause of a decrease in seismic anisotropy with depths in the upper mantle. To better understand upper mantle seismic signals, we investigate the origin of E-type fabrics using a natural olivine by deformation experiments. An olivine crystal was first hydrated at 5 GPa and 1473 K (with 4-60 ppm H_2O), or dehydrated at room pressure at 1473 K at an oxygen fugacity near the enstatite-magnesite-olivine-graphite (EMOG) buffer. This hydrated/dehydrated olivine was then sheared in the [100] direction on the (001) plane at pressures of 2 to 5 GPa and temperatures of 1473 or 1573 K. The deformed samples were observed by transmission electron microscopy (TEM) on the (001) plane to determine whether the [100](001) slip system was activated or not. Only ***c***-elongated [100] dislocations were observed for the anhydrous samples, while [100](001) dislocations dominated in the hydrous samples. The dislocation structure of the [100](001) slip system developed under hydrous and relatively low-temperature conditions and is different from the slip mechanisms detected under anhydrous and high-temperature conditions in previous studies. We conclude that the incorporation of water into olivine helps activate the [100](001) slip system by reducing its Peierls stress. This supports the idea that E-type fabrics can exist under hydrous conditions and that a transition to this fabric may be the cause of seismic anisotropy decrease with depth in the asthenosphere.

Keywords: slip system, E-type olivine fabric, hydrous olivine, TEM, dislocation structure

Introduction

Crystallographic preferred orientation (CPO), or fabric, of olivine is essential to interpret the seismic anisotropy in the Earth's upper mantle (Wenk and Van Houtte, 2004, Mainprice 2007,

Karato et al., 2008), because olivine is the most abundant mineral in the upper mantle (Ringwood, 1991), and is elastically anisotropic (Kumazawa and Anderson, 1969). Olivine CPOs change according to physical and chemical environments, as suggested by observations of natural samples and laboratory deformation experiments. Therefore, knowledge of conditions of fabric formation can be used to understand physical and chemical conditions in the Earth's interior. Moreover, mantle flow geometry can be inferred by combining observations of seismic anisotropy with knowledge of CPO formation of mantle minerals.

A number of seismic studies have shown that seismic anisotropy in the upper mantle becomes weaker with depth. One-dimensional global models, PREM (Dziewonski and Anderson, 1981) and SP6-F (Montagner and Kennett, 1996), suggested that horizontally polarized S-wave velocity (V_{SH}) is faster than vertically polarized S-wave velocity (V_{SV}) in the uppermost mantle, but this difference decreases with depth. The V_{SH}/V_{SV} ratio obtained from shear wave tomography (Gung et al., 2003) and surface wave analyses (Visser et al., 2008) reached identical conclusions. The decrease in seismic anisotropy may reflect a change of olivine CPO due to different thermomechanical conditions.

Conditions of formation of different CPOs in olivine aggregates have been studied by both petrography and experiments. Lineation and foliation of peridotite are believed to represent the shear direction and shear plane of mantle flow, respectively. By this assumption, olivine fabrics can be identified for natural samples. Mainprice (2007) categorized olivine CPO types to six different groups (A, B, C, D, E, AG) using dataset from Ismaïl and Mainprice (1998) and found that most peridotite samples from ophiolites and the continental lithosphere show A-type olivine fabrics. Tommasi and Vauchez (2015) used enlarged dataset and found that the E-type fabric has been

observed only in harzburgite and dunite deformed under hydrous conditions. These investigations suggested that water can cause A- to E-type fabric transition. This idea is also supported by Michibayashi et al. (2016). They demonstrated that the E-type fabrics were not found in ridge peridotites, by investigating their recently compiled dataset. The V_{SH}/V_{SV} ratios produced by the E-type fabric are smaller than by those formed by the A-type fabric (Karato et al., 2008). Since asthenosphere contains more water than lithosphere (Hirth and Kohlstedt, 1996), the possible water-induced A- to E-type fabric transition can explain why the seismic anisotropy decreases with depth.

Laboratory deformation experiments also suggested water-induced fabric transitions. Jung and Karato (2001) suggested that the olivine fabric changes from A- to C-type with increasing water content. Katayama et al. (2004) suggested that E-type fabric dominates at moderate water content between the A- and C-type fabrics. They reported that the boundaries between A- and E-type fabrics and between E- and C-type fabrics are located at water contents of 200 and of 500 to ~1100 ppm H/Si, respectively. They also suggested that the water content for the E- to C-type transition decreases with increasing stress.

Formation of CPO in mantle minerals is a consequence of the dominant slip systems in dislocation creep. The water-induced fabric transitions of olivine indicate that different slip systems dominate at different water contents. The A-, C-, E-type fabrics are assumed to be caused by the dominant activities of [100](010), [001](100) and [100](001) slip systems, respectively (Mainprice, 2007). Transmission electron microscopy (TEM) studies of natural (Goetze and Kohlstedt, 1973) and laboratory deformed samples (Darot and Gueguen, 1981; Durham and Goetze, 1977; Durham et al., 1977; Kohlstedt and Goetze, 1974; Ohuchi et al., 2015; Phakey et al., 1972) confirmed the

existence of [100](010) slip system under anhydrous conditions. The [001](100) slip system has been observed in laboratory deformed samples at high (>1523 K, Durham et al., 1977; Bai and Kohlstedt, 1992) or low temperatures (<1523 K, Gaboriaud et al., 1981; Mussi et al., 2014; Ohuchi et al., 2015; Phakey et al., 1972) under anhydrous conditions and low temperatures under hydrous conditions (Jung et al., 2006) by TEM or oxidation decoration methods. The [100](001) slip system has been observed by TEM (Durham et al., 1977) and oxidation decoration techniques (Bai and Kohlstedt, 1992; Durham et al., 1977) on laboratory deformed samples under anhydrous conditions. However, there is no TEM study to confirm the activation of [100](001) slip system under hydrous conditions, and the physical mechanisms for the existence of the E-type fabric under hydrous conditions is therefore unknown. In this study, we have therefore conducted TEM observations on hydrous olivine single crystal sheared in the [100] direction on the (001) plane to investigate a reason for the activation of the [100](001) slip system.

Experimental Procedure

Sample Preparation

The samples used in this study were single crystals of natural olivine from Pakistan. The same olivine has been described by Gose et al. (2010), which reported its major and trace element contents including its water content. Dislocation density in such olivine was determined by oxidation method (Karato, 1987). The ***c***-axis of each crystal was determined using a Huber single-crystal diffractometer operated by SINGLE2014 (Angel and Finger, 2011). The oriented olivine crystals were mounted in epoxy resin with the (001) plane exposed to the surface, and then polished using diamond powder with a grain size of 0.25 μm. The [010] and [100] axes of the

crystals were determined by means of electron backscatter diffraction (EBSD). The cube with 1.5 mm edge length was shaped from the oriented crystal along its principal crystallographic planes.

Hydration/dehydration experiments

The olivine cubes were hydrated or dehydrated before deformation. In dehydration, the cubes were put into a Pt basket and annealed at ambient pressure and a temperature of 1473 K for 12 h in a CO-CO_2 gas mixing furnace. The oxygen partial pressure was controlled at $10^{-7.5}$ MPa, which was near the enstatite-magnesite-olivine-graphite (EMOG) buffer.

Hydration experiments were conducted at a pressure of 5 GPa and a temperature of 1473 K using a Kawai-type multi-anvil apparatus at University of Bayreuth. The cell assembly is shown in Fig. 1. A single-crystal olivine cube was loaded into a gold capsule with outer and inner diameters of 3.7 and 3.2 mm, respectively, whose one end was sealed. A mixture of talc and brucite powders (weight ratio 4:1) was loaded at the sealed end of the capsule. It was used as a water source and also to control the silica activity of the sample. Graphite powder was used to surround the cube to prevent its mechanical damage during compression and to constrain the oxygen fugacity inside the capsule under the EMOG buffer conditions. Various water contents in the samples were obtained by having different ratios of the water source to graphite. The open end of the capsule was closed and sealed by arc welding after sample loading. The gold capsule was located in an MgO cylinder in a graphite stepped heater with a ZrO_2 thermal insulator. Tungsten carbide anvils with a 15 mm truncated edge length were used to generate high pressure together with a Cr_2O_3-doped MgO octahedron with a 25 mm edge length as a pressure medium. Sample pressures were estimated from the hydraulic oil pressure based on calibrations using the phase transitions of Bi and Mg_2SiO_4

polymorphs. Temperatures were measured using a W97%Re3%-W75%Re25% thermocouple whose junction was located near one end of the capsule. The sample was pressurized to 5 GPa in 4 h, heated to a temperature of 1473 K at a rate of 50 K/min, and kept at this temperature for 16 h. After annealing, the sample was quenched by switching off the heating power, and decompressed to ambient pressure in 16 h. After hydration, the sample was shaped as a cube with edge length of 1 to 1.2 mm to remove the graphite and magnesite on the surface.

Deformation experiments

Deformation experiments were conducted using a Kawai-type multi-anvil apparatus at pressures of 2 to 5 GPa and temperatures of 1473 and 1573 K. Figure 2 shows the experimental setup. A square hole was made at the center of an MgO slice to accommodate the cubic olivine crystal in a unique orientation. The MgO slice with the olivine crystal was sandwiched between two crushable alumina pistons. The shear geometry was in the [100] direction on the (001) plane. In order to prevent dehydration of hydrated olivine at high temperatures, thin layers of talc + brucite mixtures were put between the MgO slice and alumina pistons in the deformation experiments under hydrous conditions. The sample and pistons were placed in a welded Pt capsule. Two columns of crushable alumina were placed on both ends of the capsule. The other parts of assembly were the same as those used in the hydration experiments.

The cell assembly was first pressurized to a target pressure at ambient temperature in 4 h. A target temperature was reached in 15 min, and kept constant for 15 min to sinter the crushable alumina. The sample was then further compressed by increasing press load of 0.2 MN in 15 min to deform the sample. After the deformation, the sample was quenched by switching off the heating

power, and then decompressed to ambient pressure for more than 16 h. The same experimental set up and deformation step were employed in our previous studies (Wang et al., 2016, Wang et al., 2017) and succeeded in activating [100](010) and [001](010) slip systems in olivine. Therefore, we think that the experimental set up and procedure are suitable for present study.

FT-IR measurements

Water contents of the samples before and after deformation were determined by un-polarized FT-IR spectroscopy with 200 scans for each spectrum at a resolution of 1 cm^{-1}. Spectra were taken at the rim and center of the sample after deformation to investigate the water distribution inside the sample. The light paths were perpendicular to the (010) planes of the samples. Paterson (1982) calibration was used for calculation of the water contents in order to directly compare our results with those obtained by Jung and Karato (2001) and Katayama et al. (2004).

TEM observation

The deformed samples were double-side polished parallel to the (001) planes to thicknesses ranging from 23 to 35 μm and fixed on glass slides. After removing olivine from the glass slide, an Ar ion-milling method was used to make the sample thinner, with a voltage of 4.5 kV and incident angles of 4 to 8º from the top and bottom of the ion-bombardment, and the total thinning time varying between 14 to 25 h depending on the thicknesses and size of each sample. TEM observations were performed with a FEI Titan G2 80-200 S/TEM equipped with 4 silicon drift detectors for energy-dispersive X-ray spectrometry, operating at an acceleration voltage of 200 kV. Dislocation microstructures were examined by dark-field (DF, Bragg condition, deviation parameter,

175 s = 0) and weak-beam dark-field (WBDF, s > 0) imaging and selected-area electron diffraction
176 (SAED). We chose diffraction vectors with **g** = 400 to observe the [100] dislocations which should
177 be the Burgers vector of the deformed olivine in the [100] direction on the (001) plane. If there are
178 [100](001) dislocations, they should be visible as elongated dislocation lines on the plane. We
179 measured the total length of dislocation lines per area and calculated a dislocation density based on
180 the assumption that the thickness of the TEM foils is 250 nm.
181
182 **Results**
183 Table 1 shows the experimental conditions together with the water content of the samples
184 before and after deformation. The FT-IR spectra of hydrous samples before and after deformation
185 were shown in Fig. 3. The dominant OH bands are at 3613, 3590 and 3569 cm^{-1}.The water contents
186 in these samples increased only slightly after deformation, indicating that a small amount of water
187 was absorbed from the layers of talc and brucite mixture during deformation. Water was
188 homogeneously distributed in the samples as is seen from the fact that the FT-IR spectra in the
189 center and rim of the crystals are almost identical (Fig. 3). The water contents in the samples are
190 below the water solubility in olivine (Kohlstedt et al., 1996).
191 Stresses during experiments were estimated from the dislocation density using the relationship
192 between dislocation density and stresses given by Karato and Jung (2003). The dislocation density
193 and estimated stresses are given in Table 1. There is nearly no dislocations in the initial undeformed
194 olivine. Therefore, the production of dislocations indicated that deformation of sample occurred
195 during the deformation experiments.

196 TEM images of dislocations activated under anhydrous conditions are shown in Fig. 4. The
197 sample after deformation contained water less than 80 ppm H/Si, which falls into the region of
198 A-type fabric in Katayama et al. (2004). We found only dislocations with the Burgers vector of [100]
199 elongated in the [001] direction in these samples. No line contrast of dislocations was observed on
200 the (001) plane, indicating that (001) is not a slip plane under the experimental conditions.
201 Typical dislocation microstructures activated under hydrous conditions are shown in Fig. 5.
202 Dislocation lines and loops with the Burgers vector of [100] were observed on the (001) plane,
203 suggesting that the [100](001) slip system was activated. The majority of dislocation lines elongate
204 in the [010] direction, indicating their edge characters. The dislocation loops consist of long edge
205 segment (***b***-elongated) and short screw segment (***a***-elongated), indicating lower mobility of the edge
206 components in comparison with the screw components. Some screw dislocations have cross-slipped
207 (Fig 5c). Edge dipoles due to motion of such dislocations can be seen (Fig. 5c, 5d). Some [010]
208 elongated dislocation loops are observed (Fig 5c), which are likely to be debris of motion of
209 cross-slipped screw dislocations. The [100] short edge dislocations are likely to be dislocations on
210 other (0kl) slip planes (e.g. Green and Radcliffe, 1972). The [100] dislocations elongated to the [001]
211 directions, which are dominant under anhydrous conditions, also exist.
212
213 **Discussion**
214 *Comparison of the dislocation microstructures with previous studies*
215 The [100](001) slip system has been reported in previous studies (Durham et al., 1977; Bai and
216 Kohlstedt 1993) under anhydrous and high-temperature (>1623 K) conditions. Durham et al. (1977)
217 reported that [100] dislocations exhibit a peculiar microstructure with zigzag line configurations

corresponding to the stabilization of <110> segments. Bai and Kohlstedt (1992) found that the dislocation structures developed at high oxygen fugacity are the same as those in Durham et al. (1977). At low oxygen fugacity, Bai and Kohlstedt (1992) found that the dislocation configuration consists of long straight screw and short curved edge segments. The dislocation configuration developed under hydrous conditions in the present study is quite different from these previous studies. Dislocations developed under hydrous conditions in this study consist of long edge and short curved screw segments instead of long straight screw and short curved edge dislocations, indicating that glide velocity of screw dislocation is more enhanced by water incorporation than that of edge dislocations. Moreover, no <110> zigzag edge dislocation line was observed in the present study. Instead, edge dislocation lines are curved. The observations that dislocation lines are generally curved indicate that the Peierls stress for this slip system is reduced by water incorporation and dislocation glide velocity is enhanced.

Crystallographic sites of H incorporation

The identical band positions in FTIR spectra at different stages of the experiments (Fig. 3) indicate that OH defect structures did not change during experiments. The OH point defects in the sample were controlled by the hydration experiments since the deformation experiments only lasted for 15 min. The group I OH bands (Bai and Kohlstedt, 1992) are dominant in this study. Although some earlier studies (e.g. Matveev et al., 2001; Matveev et al., 2004; Lemaire et al., 2004) suggested that the group I bands should not dominate at high silica activity buffered sample, later studies (e.g. Smyth et al., 2006) suggested that silica activity has minimal effect on the sites of H incorporation at high pressures. In addition, the band positions in this study are consistent with

those in previous studies that performed at similar thermodynamic conditions (e.g. Kohlstedt et al., 1996; Mosenfelder et al., 2006; Kovacs et al., 2010) within the resolution of the spectrometer. Therefore, the OH defect structures reached equilibrium at the present experimental conditions.

Recent first principle calculation studies (Balan et al. 2011; Umemoto et al. 2011) indicated that group I bands reflect the hydration of Si vacancy. Thus, we conclude that most H are incorporated at Si vacancies in this study.

The possible mechanism of activation of the [100](001) slip system due to water incorporation

Our TEM results suggested that incorporation of water activate (001) slip plane. The reason for this activation is still unclear and needs dislocation core modelling at the atomic scale (e.g. Mahendran et al., 2017). Nevertheless, we provide a tentative explanation. The olivine structure has an orthorhombic symmetry with the space group *Pbnm*. This structure has three different oxygen sites (O1, O2, O3), two different metal sites (M1, M2) and one silicon site. O1, O2, M2 and Si lie on mirror planes, while M1 lies on an inversion center. O3 lies in a general position (Fig. 6). A slip on the (001) plane needs to cut Si-O or/and M-O bonds (Fig. 6). H incorporation leads to an increase of Si vacancies (Brodholt and Refson, 2000). In addition, the dominant group I bands in this study indicate that H^+ replaces Si^{4+} (Balan et al. 2011; Umemoto et al. 2011.). Either Vacancy-O bond or H-O bond must be much weaker than Si-O bonds. Therefore, incorporation of H facilitate of (001) as a slip plane. For comparison, the (010) slip plane can only cut M-O bonds (Fig. 6). Since H mainly influence Si vacancy, dislocation motions on (010) plane should not be enhanced as much as dislocation motions on (001) plane, which is consistent with previous deformation experiments (e.g. Katayama et al., 2004).

Implications

The decrease of seismic anisotropy with depth in the mantle has been observed in several studies (Dziewonski and Anderson, 1981; Gung et al., 2003; Montagner and Kennett, 1996; Nettles and Dziewonski, 2008; Visser et al., 2008). One explanation is that olivine fabric changes from A- to E-type due to water (Katayama et al., 2004; Karato et al., 2008). However, the [100](001) slip system was only reported in deformation experiments under anhydrous conditions (Bai and Kohlstedt, 1992; Durham et al., 1977). Whether this slip system can be activated under hydrous conditions was unclear before the present study. Our TEM observation of the samples deformed under anhydrous and hydrous conditions suggests that water facilitates activation of the [100](001) slip at relatively low temperatures. The physical reason for the activation is the reduction of Peierls stresses because of water incorporation, which was revealed by the dislocation structures. Therefore, the E-type fabric can exist under hydrous conditions. Since water content in olivine increases with depth (Katsura et al., 2017), the contribution of E-type fabric to seismic anisotropy should increase with depth and the weak seismic anisotropy of the asthenosphere could be explained by the predominance of this fabric.

Acknowledgements

We acknowledge F. Heidelbach and P. O'Brien for providing the olivine single crystals and T. Boffa-Ballaran for instructing the single crystal X-ray diffractometry. We thank technicians in BGI for the sample and assembly preparation. This research was supported by DFG grants to TK (KA3434/3-1, KA3434/7-1, KA3434/8-1 and KA3434/9-1) and by the annual budget of BGI.

References

Angel, R., and Finger, L. (2011) SINGLE: a program to control single-crystal diffractometers. Journal of Applied Crystallography, 44(1), 247-251.

Bai, Q., and Kohlstedt, D.L. (1992) High-temperature creep of olivine single crystals, 2. dislocation structures. Tectonophysics, 206(1–2), 1-29.

Bai, Q., and Kohlstedt, D. (1993) Effects of chemical environment on the solubility and incorporation mechanism for hydrogen in olivine. Physics and Chemistry of Minerals, 19(7), 460-471.

Balan, E., Ingrin, J., Delattre, S., Kovács, I., and Blanchard, M. (2011) Theoretical infrared spectrum of OH-defects in forsterite. European Journal of Mineralogy, 23(3), 285-292.

Bell, D.R., Rossman, G.R., Maldener, J., Endisch, D., and Rauch, F. (2003) Hydroxide in olivine: A quantitative determination of the absolute amount and calibration of the IR spectrum. Journal of Geophysical Research-Solid Earth, 108(B2), 9.

Brodholt, J.P., and Refson, K. (2000) An ab initio study of hydrogen in forsterite and a possible mechanism for hydrolytic weakening. Journal of Geophysical Research: Solid Earth, 105(B8), 18977-18982.

Darot, M., and Gueguen, Y. (1981) High‐temperature creep of forsterite single crystals. Journal of Geophysical Research: Solid Earth, 86(B7), 6219-6234.

Durham, W.B., and Goetze, C. (1977) A comparison of the creep properties of pure forsterite and iron-bearing olivine. Tectonophysics, 40(3), T15-T18.

Durham, W.B., Goetze, C., and Blake, B. (1977) PLASTIC-FLOW OF ORIENTED SINGLE-CRYSTALS OF OLIVINE .2. OBSERVATIONS AND INTERPRETATIONS OF DISLOCATION-STRUCTURES. Journal of Geophysical Research, 82(36), 5755-5770.

Dziewonski, A.M., and Anderson, D.L. (1981) Preliminary reference Earth model. Physics of the Earth and Planetary Interiors, 25(4), 297-356.

Gaboriaud, R., Darot, M., Gueguen, Y., and Woirgard, J. (1981) Dislocations in olivine indented at low temperatures. Physics and Chemistry of Minerals, 7(2), 100-104.

Goetze, C., and Kohlstedt, D.L. (1973) Laboratory study of dislocation climb and diffusion in olivine. Journal of Geophysical Research, 78(26), 5961-5971.

Gose, J., Schmaedicke, E., Markowitz, M., and Beran, A. (2010) OH point defects in olivine from Pakistan. Mineralogy and Petrology, 99(1-2), 105-111.

Green, H., and Radcliffe, S. (1972) Dislocation mechanisms in olivine and flow in the upper mantle. Earth and Planetary Science Letters, 15(3), 239-247.

Gung, Y., Panning, M., and Romanowicz, B. (2003) Global anisotropy and the thickness of continents. Nature, 422(6933), 707-711.

Hirth, G., and Kohlstedt, D.L. (1996) Water in the oceanic upper mantle: implications for rheology, melt extraction and the evolution of the lithosphere. Earth and Planetary Science Letters, 144(1–2), 93-108.

Ismaïl, W.B., and Mainprice, D. (1998) An olivine fabric database: an overview of upper mantle fabrics and seismic anisotropy. Tectonophysics, 296(1–2), 145-157.

Jamtveit, B., Brooker, R., Brooks, K., Larsen, L.M., and Pedersen, T. (2001) The water content of olivines from the North Atlantic Volcanic Province. Earth and Planetary Science Letters, 186(3-4), 401-415.

328 Jung, H., and Karato, S.-i. (2001) Water-Induced Fabric Transitions in Olivine. Science, 293(5534),
329 1460-1463.
330 Jung, H., Katayama, I., Jiang, Z., Hiraga, T., and Karato, S. (2006) Effect of water and stress on the
331 lattice-preferred orientation of olivine. Tectonophysics, 421(1–2), 1-22.
332 Karato, S. (1987) Scanning electron microscope observation of dislocations in olivine. Physics and
333 Chemistry of Minerals, 14(3), 245-248.
334 Karato, S.-I., and Jung, H. (2003) Effects of pressure on high-temperature dislocation creep in
335 olivine. Philosophical Magazine, 83(3), 401-414.
336 Karato, S.-i., Jung, H., Katayama, I., and Skemer, P. (2008) Geodynamic Significance of Seismic
337 Anisotropy of the Upper Mantle: New Insights from Laboratory Studies. Annual Review of
338 Earth and Planetary Sciences, 36(1), 59-95.
339 Katayama, I., Jung, H., and Karato, S.-i. (2004) New type of olivine fabric from deformation
340 experiments at modest water content and low stress. Geology, 32(12), 1045-1048.
341 Katsura, T., Baba, K., Yoshino, T., and Kogiso, T. (2017) Electrical conductivity of the oceanic
342 asthenosphere and its interpretation based on laboratory measurements. Tectonophysics, 717,
343 162-181.
344 Kohlstedt, D., Keppler, H., and Rubie, D. (1996) Solubility of water in the α, β and γ phases of (Mg,
345 Fe) 2SiO4. Contributions to Mineralogy and Petrology, 123(4), 345-357.
346 Kohlstedt, D.L., and Goetze, C. (1974) Low-stress high-temperature creep in olivine single crystals.
347 Journal of Geophysical Research, 79(14), 2045-2051.
348 Kovacs, I., O'Neill, H.S.C., Hermann, J., and Hauri, E.H. (2010) Site-specific infrared O-H
349 absorption coefficients for water substitution into olivine. American Mineralogist, 95(2-3),
350 292-299.
351 Kumazawa, M., and Anderson, O.L. (1969) Elastic moduli, pressure derivatives, and temperature
352 derivatives of single-crystal olivine and single-crystal forsterite. Journal of Geophysical
353 Research, 74(25), 5961-5972.
354 Lemaire, C., Kohn, S., and Brooker, R. (2004) The effect of silica activity on the incorporation
355 mechanisms of water in synthetic forsterite: a polarised infrared spectroscopic study.
356 Contributions to Mineralogy and Petrology, 147(1), 48-57.
357 Mainprice, D. (2007) Seismic anisotropy of the deep Earth from a mineral and rock 1022 physics
358 perspective. Schubert, G. Treatise in Geophysics Volume 2 pp437-492. Oxford.
359 Mahendran, S., Carrez, P., Groh, S., and Cordier, P. (2017) Dislocation modelling in Mg2SiO4
360 forsterite: an atomic-scale study based on the THB1 potential. Modelling and Simulation in
361 Materials Science and Engineering, 25(5), 054002.
362 Matveev, S., O'neill, H.S.C., Ballhaus, C., Taylor, W.R., and Green, D. (2001) Effect of silica
363 activity on OH− IR spectra of olivine: implications for low-a SiO2 mantle metasomatism.
364 Journal of Petrology, 42(4), 721-729.
365 Matveev, S., Portnyagin, M., Ballhaus, C., Brooker, R., and Geiger, C. (2004) FTIR spectrum of
366 phenocryst olivine as an indicator of silica saturation in magmas. Journal of Petrology, 46(3),
367 603-614.
368 Michibayashi, K., Mainprice, D., Fujii, A., Uehara, S., Shinkai, Y., Kondo, Y., Ohara, Y., Ishii, T.,
369 Fryer, P., and Bloomer, S.H. (2016) Natural olivine crystal-fabrics in the western Pacific
370 convergence region: A new method to identify fabric type. Earth and Planetary Science
371 Letters, 443, 70-80.

Montagner, J.P., and Kennett, B.L.N. (1996) How to reconcile body-wave and normal-mode reference earth models. Geophysical Journal International, 125(1), 229-248.

Mosenfelder, J.L., Deligne, N.I., Asimow, P.D., and Rossman, G.R. (2006) Hydrogen incorporation in olivine from 2–12 GPa. American Mineralogist, 91(2-3), 285-294.

Mussi, A., Cordier, P., Demouchy, S., and Vanmansart, C. (2014) Characterization of the glide planes of the [001] screw dislocations in olivine using electron tomography. Physics and Chemistry of Minerals, 41(7), 537-545.

Nettles, M., and Dziewonski, A.M. (2008) Radially anisotropic shear velocity structure of the upper mantle globally and beneath North America. Journal of Geophysical Research-Solid Earth, 113(B2), 27.

Ohuchi, T., Kawazoe, T., Higo, Y., Funakoshi, K.-i., Suzuki, A., Kikegawa, T., and Irifune, T. (2015) Dislocation-accommodated grain boundary sliding as the major deformation mechanism of olivine in the Earth's upper mantle. Science advances, 1(9), e1500360.

Paterson, M. (1982) The determination of hydroxyl by infrared absorption in quartz, silicate glasses, and similar materials. Bulletin de la Societe Francaise de Mineralogie, 105, 20-29.

Phakey, P., Dollinger, G., and Christie, J. (1972) Transmission electron microscopy of experimentally deformed olivine crystals. Flow and Fracture of rocks, 117-138.

Ringwood, A.E. (1991) Phase transformations and their bearing on the constitution and dynamics of the mantle. Geochimica et Cosmochimica Acta, 55(8), 2083-2110.

Smyth, J.R., Frost, D.J., Nestola, F., Holl, C.M., and Bromiley, G. (2006) Olivine hydration in the deep upper mantle: Effects of temperature and silica activity. Geophysical Research Letters, 33(15).

Tommasi, A., and Vauchez, A. (2015) Heterogeneity and anisotropy in the lithospheric mantle. Tectonophysics, 661, 11-37.

Visser, K., Trampert, J., Lebedev, S., and Kennett, B.L.N. (2008) Probability of radial anisotropy in the deep mantle. Earth and Planetary Science Letters, 270(3–4), 241-250.

Umemoto, K., Wentzcovitch, R.M., Hirschmann, M.M., Kohlstedt, D.L., and Withers, A.C. (2011) A first-principles investigation of hydrous defects and IR frequencies in forsterite: The case for Si vacancies. American Mineralogist, 96(10), 1475-1479.

Wang, L., Blaha, S., Kawazoe, T., Miyajima, N., and Katsura, T. (2017) Identical activation volumes of dislocation mobility in the [100](010) and [001](010) slip systems in natural olivine. Geophysical Research Letters, 44(6), 2687-2692.

Wang, L., Blaha, S., Pintér, Z., Farla, R., Kawazoe, T., Miyajima, N., Michibayashi, K., and Katsura, T. (2016) Temperature dependence of [100](010) and [001](010) dislocation mobility in natural olivine. Earth and Planetary Science Letters, 441, 81-90.

Wenk, H.-R., and Van Houtte, P. (2004) Texture and anisotropy. Reports on Progress in Physics, 67(8), 1367.

410 **Figure and table captions**

411 Figure 1. The sample assembly used in the multi-anvil hydration experiments.

412

413 Figure 2. The sample assembly used in the multi-anvil high-pressure deformation experiments. The
414 crystallographic orientation of the olivine single crystal is also shown.

415

416 Figure 3. FT-IR spectra of samples deformed at 1473 K under hydrous conditions after base line
417 correction and thickness normalization to 1 cm. (a) sample deformed at 2 GPa. (b) sample deformed
418 at 5 GPa. The red spectra were obtained before deformation. The blue and black spectra were
419 obtained after deformation at the sample center and rim, respectively.

420

421 Figure 4. WBDF images showing character of [100] dislocations in the sample deformed under
422 anhydrous conditions. a) sample deformed at 2 GPa and 1473 K. b) sample deformed at 3 GPa and
423 1573 K. The all images were taken using **g** = 400. The [100] dislocations along the [001] direction
424 are indicated by blue arrows.

425

426 Figure 5. WBDF images showing dislocation character of sample deformed at 1473 K under
427 hydrous conditions. a) sample deformed at 2 GPa. b),c) and d) hydrous sample deformed at 5 GPa.
428 The all images were taken using **g** = 400. The [100] dislocations on the (001) plane are generally
429 curved, and kinks are shown by red arrows. Screw dislocations have cross-slips (white arrows).
430 Edge dipoles (orange arrows) and [010] elongated dislocation loops (yellow arrows) due to motion
431 of such cross-slipped dislocations can be seen. Some [100] short edge dislocations are likely on
432 other (0kl) slip planes (green arrows). The [100] dislocations along the [001] direction are indicated
433 by blue arrows.

434

435 Figure 6. Olivine structure viewed from near [100] direction. Red sticks indicate M-O bonds. Blue
436 sticks indicate Si-O bonds. The green plane shows a (001) slip plane which cut both M-O and Si-O
437 bonds. The red plane shows a (010) plane which cut only M-O bonds.

438

439

440

441 Table 1. Summary of experimental conditions and water content before and after deformation

No	*T* (K)	*P* (GPa)	Dislocation density (μm^{-2})	Stress (MPa)	Water before (ppm H/Si)	Water after (ppm H/Si)
H4477*	1473	2	0.2	40	37	61
Z1486*	1573	3	1.6	175	37	73
Z1711#	1473	5	3.5	305	863	970
Z1714#	1473	2	1.5	167	545	583

442 * Anhydrous deformation experiment. No layer of mixture of talc and brucite was added.
443 # Hydrous deformation experiment. Layers of a mixture of talc and brucite were added.

444

445

This is a preprint, the final version is subject to change, of the American Mineralogist (MSA)
Cite as Authors (Year) Title. American Mineralogist, in press.
DOI: https://doi.org/10.2138/am-2019-6574

446 Figure 1.

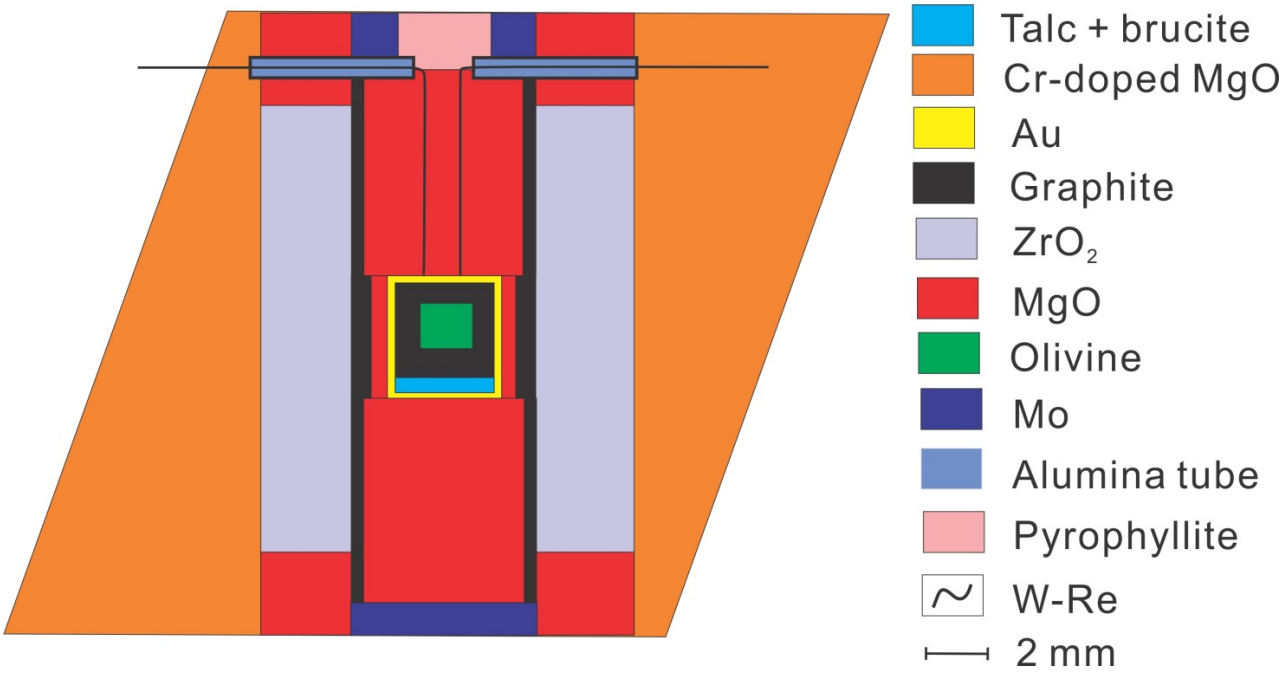

447

448

449

This is a preprint, the final version is subject to change, of the American Mineralogist (MSA)
Cite as Authors (Year) Title. American Mineralogist, in press.
DOI: https://doi.org/10.2138/am-2019-6574

450 Figure 2.

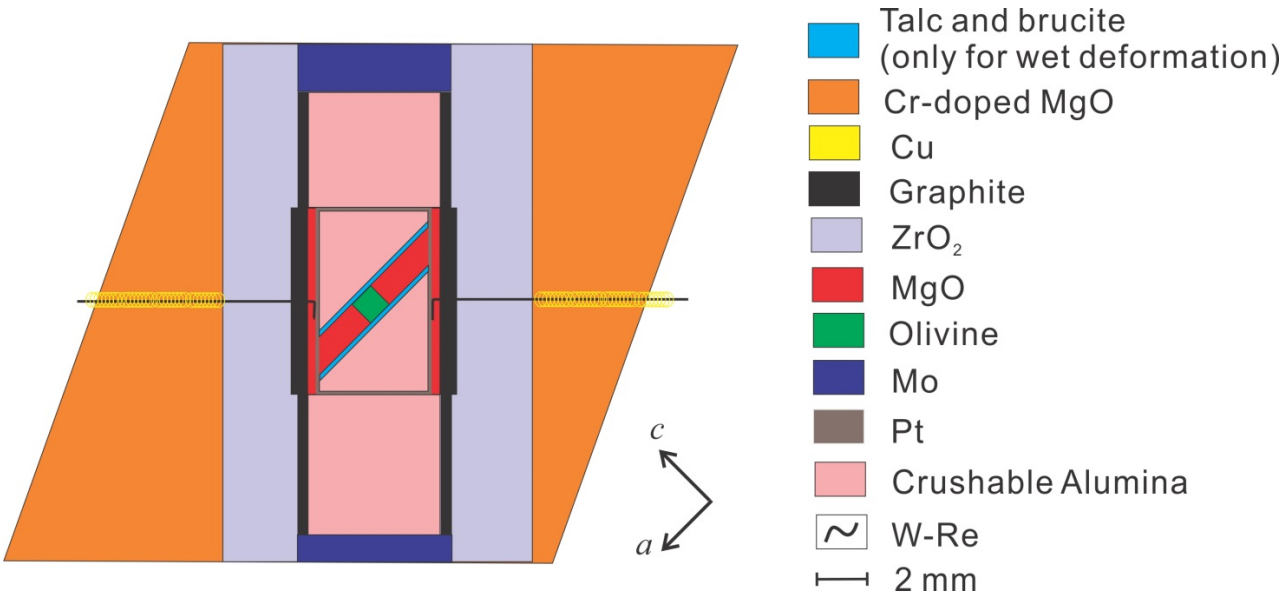

451

452

453 Figure 3

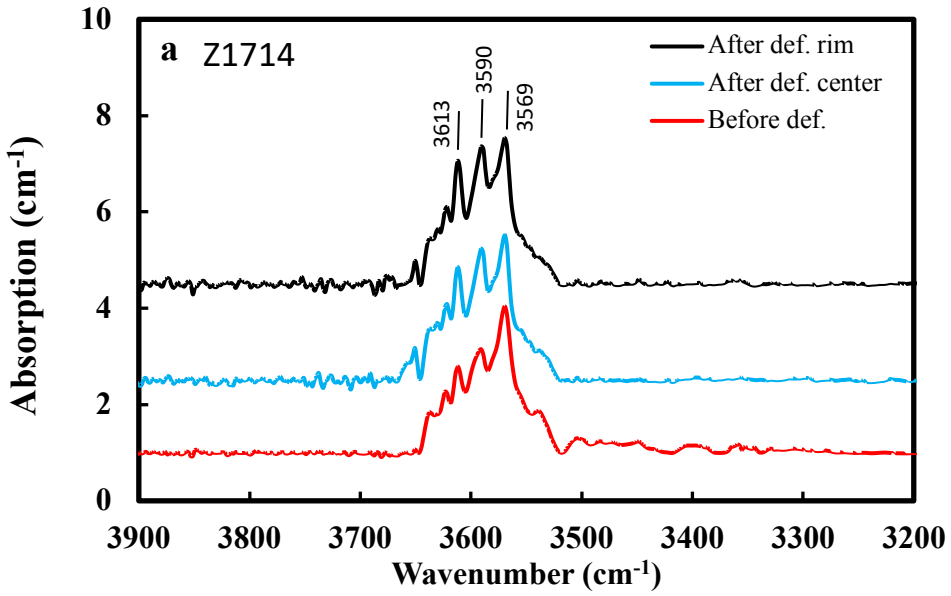

454

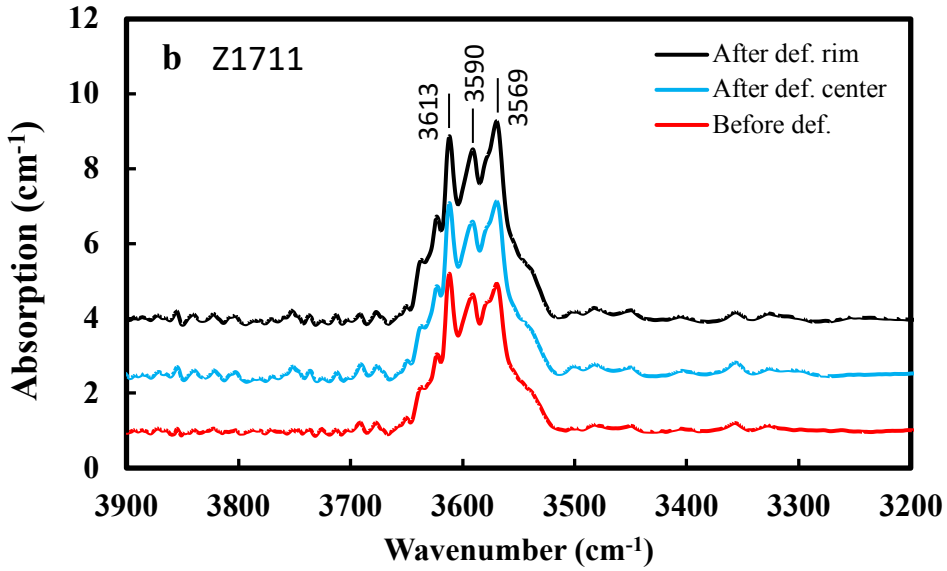

455

456

This is a preprint, the final version is subject to change, of the American Mineralogist (MSA)
Cite as Authors (Year) Title. American Mineralogist, in press.
DOI: https://doi.org/10.2138/am-2019-6574

457 Figure 4.

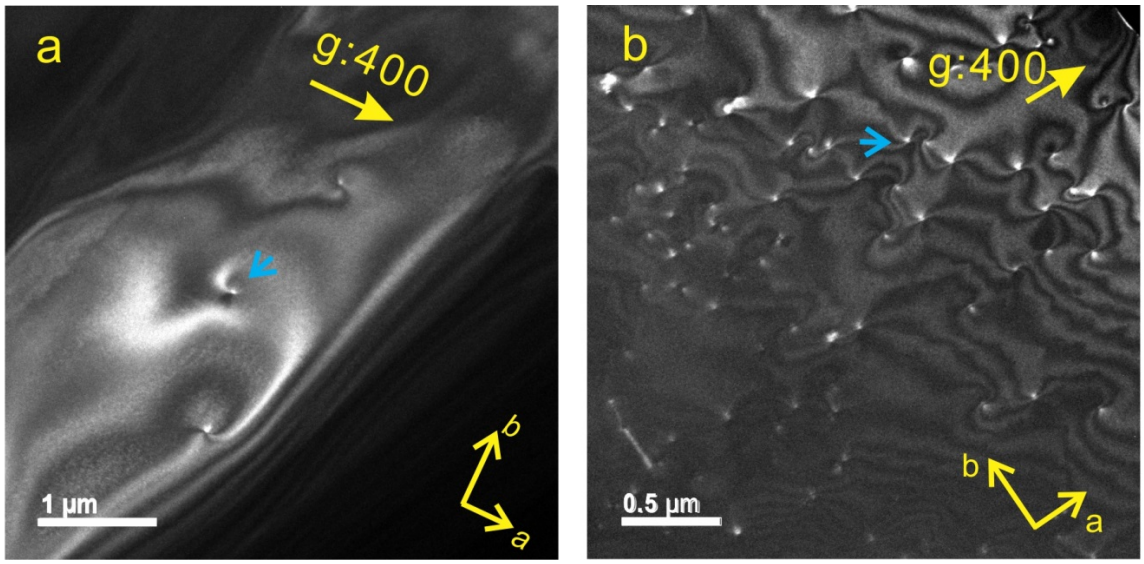

458
459

This is a preprint, the final version is subject to change, of the American Mineralogist (MSA)
Cite as Authors (Year) Title. American Mineralogist, in press.
DOI: https://doi.org/10.2138/am-2019-6574

460 Figure 5

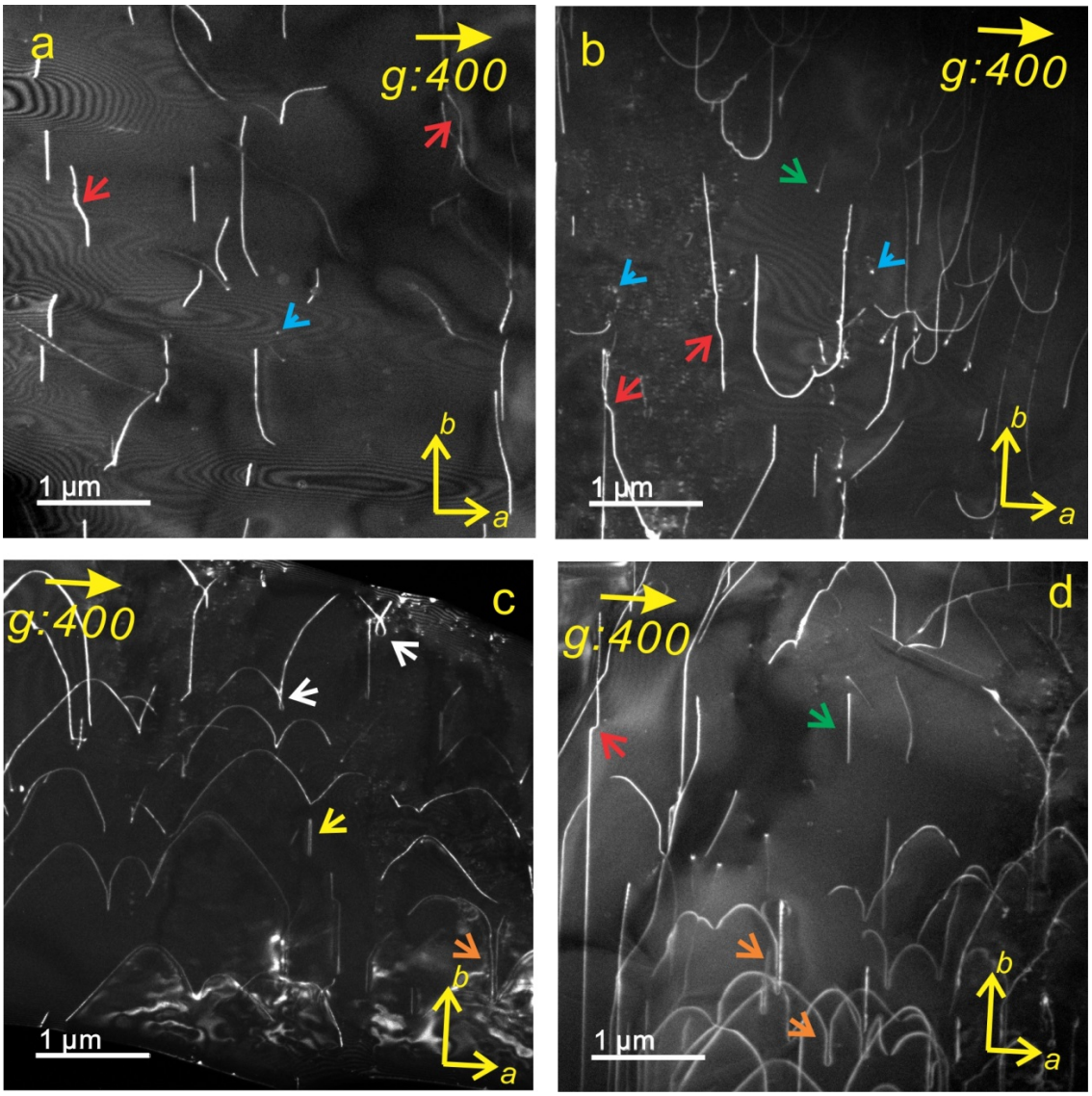

461

462

463

464 Figure 6.

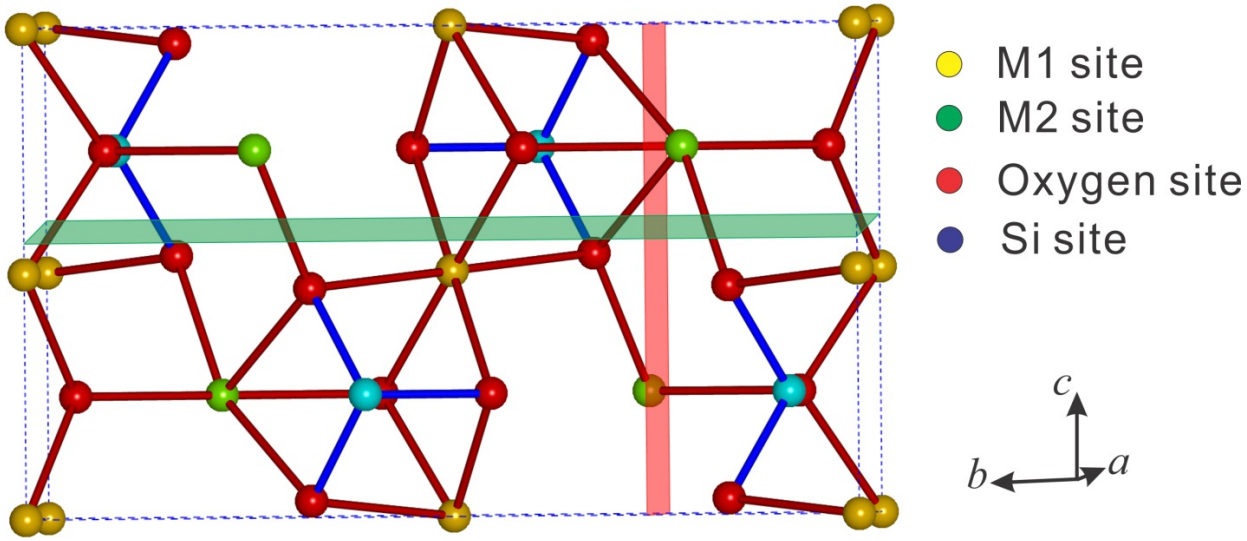

465